energies

MDPI

Article

Hybrid Vibration Reduction System for a Vehicle Suspension under Deterministic and Random Excitations

Paweł Orkisz * and Bogdan Sapiński *

Department of Process Control, Faculty of Mechanical Engineering and Robotics, AGH University of Science and Technology, Mickiewicza 30 Av., 30-059 Krakow, Poland

* Correspondence: orkisz@agh.edu.pl (P.O.); deep@agh.edu.pl (B.S.); Tel.: +48-126-173-032 (P.O.)

Abstract: This paper concerns a hybrid vibration reduction system (HVRS) equipped with a linear electrodynamic motor (LM). The objective of the study was to implement the HVRS in a scaled vehicle suspension and reveal the benefits of its application in the system. First, a mathematical model of a quarter-vehicle suspension with the HVRS was formulated. Next, the dynamic similarity method was employed to conduct numerical simulations of the passive vibration reduction system (PVRS). Subsequently, an algorithm for HVRS controlling was developed. Then, the system was investigated experimentally under deterministic and random excitations. The results confirmed the effectiveness and applicability of the proposed HVRS.

Keywords: energy saving; vibration reduction; vehicle suspension; passive system; hybrid system; dynamic similarity; signal analysis; deterministic excitation; random excitation

Citation: Orkisz, P.; Sapiński, B. Hybrid Vibration Reduction System for a Vehicle Suspension under Deterministic and Random Excitations. *Energies* **2023**, *16*, 2202. https://doi.org/10.3390/en16052202

Academic Editor: Miguel Castilla

Received: 30 January 2023
Revised: 20 February 2023
Accepted: 22 February 2023
Published: 24 February 2023

1. Introduction

The majority of vehicle models known from the literature discuss their components with greater or lesser detail. A significant number of these are mechatronic models that account for selected parts of the mechanical structure and the integrated measurement and control components. An overview of models, comprehensively describing vehicle components, can be found, e.g., in [1–3]. These models are generally used in the implementation of control systems to improve the conditions of vehicle use and the comfort of passengers, as well as to reduce the risk of damage to cargo and to simplify or eliminate decisions made by operators.

Aiming at a given control system as the criterion for distinguishing models mentioned above, one must divide models into the following groups: systems intended for installation inside the vehicle, directional control systems, drive systems, braking systems, and suspension systems. Among the models of systems intended for installation inside the vehicle, several types can be listed: the operator's seats [4,5], steering columns and wheels [6], sound amplification systems [7], or navigation systems [8]. Modelling of a directional control system can be performed concerning such aspects as improvement of the functioning of assist systems [9], automation of speed and direction selection [10], or the correctness of the trajectory defined by autonomous vehicles [11]. Modelling of drive and braking systems takes into account mechanical constructions and control systems selected for engines [12,13], compression systems [14], exhaust systems [15], assisted braking systems [16,17] or elements of the braking system [18], driver assistance systems [19,20], and elements of the car body; in particular, the elements designed to increase vehicle adherence to the road surface [21]. Models of suspension systems can be distinguished as follows: suspensions of four-wheeled vehicles, including full suspension systems [22], half suspension systems [23–26], quarter suspension systems [27–30], and suspensions of nontypical vehicles such as hyperloop capsule vehicles [31], lorry cars [32], etc.

Another common criterion for distinguishing vehicle models involves the type of control system implemented. Having this in mind, the models can be divided as follows:

passive systems [33,34], semiactive systems [35,36], active systems [37,38], and hybrid systems [39,40]. The control systems usually employ algorithms such as: PID [41], sky-hook [42], LQR [43], switching algorithms such as sliding mode control [44,45], optimal regulators [46], and adaptive regulators [47]. Typical actuators installed in hybrid vibration reduction systems are MR dampers [48], electrodynamic linear devices [49,50] or rotary devices [51], and electropneumatic or electrohydraulic actuators [52].

In the present study, the authors investigate the hybrid vibration reduction system (HVRS) implemented in a scaled quarter-vehicle suspension under harmonic or random excitation. The dynamic similarity method was applied, considering the similarity scales of mass, time, and displacement. Furthermore, the control algorithm for HVRS controlling was modified to that described in [37]. The modification also expands the HVRS to operate under random excitations. The engineering significance of the study is to elaborate and implement the HVRS control algorithm in the test rig, taking into account all proposed similarity scales simultaneously and developing appropriate modifications in the algorithm of the excitation generation.

The paper is structured as follows. Section 2 presents a mathematical model of a quarter-vehicle suspension with a linear motor (LM), the selection of the parameters of the reference object subjected to scaling, the description of the scaling method used, and the parameters of the model on the laboratory scale. Section 3 describes numerical simulations carried out to verify the similarity of the reference object to the models and to verify the correct operation of the HVRS control algorithm subjected to deterministic and random excitations. Section 4 discusses the results of experiments carried out on a test rig, which confirm the possibility of practical implementation of the proposed algorithm. Summary results and conclusions are provided in Section 5.

2. Modelling

Let us consider a model of a simplified quarter-vehicle suspension with a LM (see diagram in Figure 1). The passive vibration reduction system (PVRS) model has two degrees of freedom. The first degree is mapped by the displacement x_1 of the unsprung mass m_1, which represents the tyre, hub, and steering knuckle. The second degree is mapped by a displacement x_2 and takes into account the movement of the chassis elements not mentioned above and body elements with a total mass of m_2 (sprung mass). The movement of the masses m_1 and m_2 takes place along one axis and is limited by the action of a spring and a shock absorber with an elasticity coefficient k_2 and a damping coefficient b_2, respectively. The spring with the elasticity coefficient k_1 and the shock absorber with the damping coefficient b_1 are responsible for the behaviour of the wheel rolling on the road surface. The excitation input in the model is a displacement z determining the impact of the vertical road profile on which the vehicle moves. Taking into account the forces F_{g1} and F_{g2} resulting from the impact of gravity on the masses m_1 and m_2 and regardless of the force F_m (LM impact), the PVRS diagram is shown in Figure 1a.

2.1. Mathematical Model

The objective of the HVRS is to reduce the vibration of the mass m_2. The actuator in the system is the LM (see Figure 1), which affects the suspension with force F_m. This force depends on the product of the current i_m in the electrical circuit LM and the force sensitivity factor κ_1. The mechanical subsystem of the HVRS is governed by the equations:

$$\begin{cases} m_1\ddot{x_1} + b_1(\dot{x_1} - \dot{z}) + b_2(\dot{x_1} - \dot{x_2}) + k_1(x_1 - z) + k_2(x_1 - x_2) = -F_m - F_{g1} \\ m_2\ddot{x_2} + b_2(\dot{x_2} - \dot{x_1}) + k_2(x_2 - x_1) = F_m - F_{g2} \end{cases} \quad (1)$$

where g is the standard acceleration of gravity and forces F_m, F_{g1}, and F_{g2} are defined as follows:

$$\begin{cases} F_m = \kappa_1 i_m \\ F_{g1} = m_1 g \\ F_{g2} = m_2 g \end{cases} \quad (2)$$

The electrical subsystem (Figure 1b) is represented by a two-terminal network with parameters R_m, L_m, and e_m, where R_m and L_m are the resistance and inductance of the LM coil, respectively, and e_m is the electromotive force proportional to the product of the relative velocity $\dot{x_1} - \dot{x_2}$ and the back emf coefficient κ_2. In the subsystem, there is also a controlled potentiometer with a resistance of R_a, a voltage regulator (VR) producing a voltage of u_m, and a relay SW. The relay disconnects the VR in the case where $u_m = 0$ V. The electrical subsystem is governed by the equations:

$$\begin{cases} u_m = L_m \dot{l_m} + R_m i_m - e_m & \forall\, u_m \neq 0 \\ e_m = R_a i_m + L_m \dot{l_m} + R_m i_m & \forall\, u_m = 0 \\ e_m = \kappa_2 \left(\dot{x_1} - \dot{x_2} \right) \end{cases} \tag{3}$$

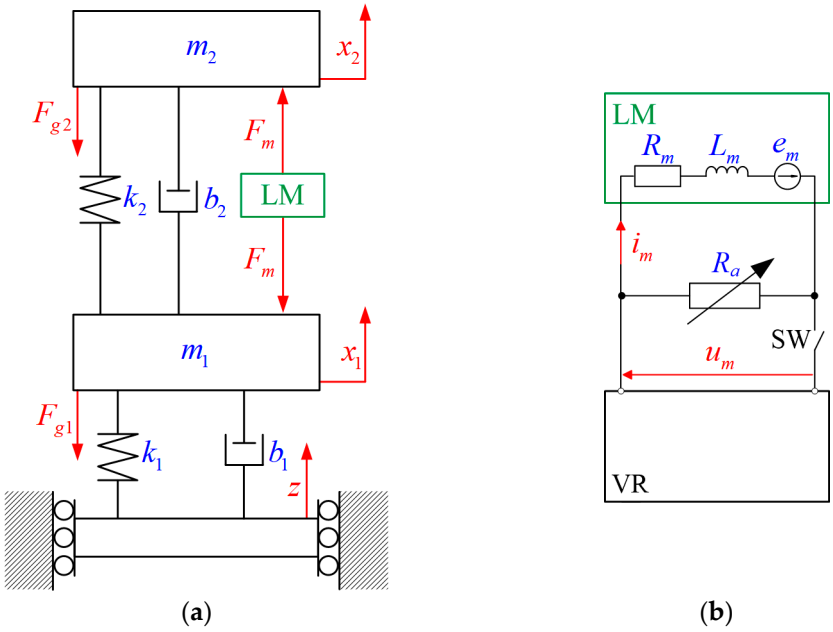

(**a**) (**b**)

Figure 1. Diagram of the HVRS: (**a**) mechanical subsystem; (**b**) electrical subsystem.

2.2. Dynamic Similarity

The dynamic similarity of the two models assumes the similarity of selected physical quantities that are important in the mathematical description of the considered system or process [53]. These quantities can be referred to as criteria numbers. The model of a quarter-vehicle suspension denoted by Equations (1)–(3) requires the introduction of three fundamental reference quantities: characteristic mass M, characteristic time T, and characteristic displacement L [54]. Taking into account Equation (1) and the set of basic quantities $\{m_1, b_1, k_1, m_2, b_2, k_2, F_m, g\}$, the following criteria numbers are established:

$$\begin{aligned} K_m &= m_2 M^{-1} \\ K_k &= k_2 T^2 M^{-1} \\ K_b &= b_2 T M^{-1} \\ K_f &= F_m T^2 M^{-1} L^{-1} \\ K_g &= m_2 g T^2 M^{-1} L^{-1} \end{aligned} \tag{4}$$

The introduced criteria numbers can also be written in a form which is simpler to physically interpret as the following relations: elasticity forces and fictitious forces, damping

forces and fictitious forces, LM interaction forces and fictitious forces, and gravity forces and fictitious forces:

$$\begin{array}{l} K_k = \frac{k_2 L}{m_2 L T^{-2}} K_m \\ K_b = \frac{b_2 L T^{-1}}{m_2 L T^{-2}} K_m \\ K_f = \frac{F_m}{m_2 L T^{-2}} K_m \\ K_g = \frac{m_2 g}{m_2 L T^{-2}} K_m \end{array} \tag{5}$$

These criteria numbers are complemented by dimensionless similarity coefficients defining the mass, damping, and stiffness ratios determined for a wheel in relation to the equivalents determined for sprung mass:

$$\alpha_m = \frac{m_1}{m_2},\ \alpha_b = \frac{b_1}{b_2},\ \alpha_k = \frac{k_1}{k_2} \tag{6}$$

Assuming dimensionless displacements in the form $\widetilde{z} = zL^{-1}$, $\widetilde{x}_1 = x_1 L^{-1}$, $\widetilde{x}_2 = x_2 L^{-1}$, and dimensionless time $\tau = tT^{-1}$, Equations (1), (5) and (6) can be used to define a dimensionless equation of motion:

$$\begin{cases} K_m \alpha_m \frac{d^2 \widetilde{x}_1}{d\tau^2} + K_b \left(\frac{d\widetilde{x}_1}{d\tau} - \frac{d\widetilde{x}_2}{d\tau} + \alpha_b \frac{d\widetilde{x}_1}{d\tau} - \alpha_b \frac{d\widetilde{z}}{d\tau} \right) + K_k (\widetilde{x}_1 \quad -\widetilde{x}_2 + \alpha_k \widetilde{x}_1 - \alpha_k \widetilde{z}) = \\ \qquad\qquad\qquad\qquad\qquad\qquad\qquad\qquad\qquad\qquad\qquad\qquad = -K_f - \alpha_m K_g \\ K_m \frac{d^2 \widetilde{x}_2}{d\tau^2} + K_b \left(\frac{d\widetilde{x}_2}{d\tau} - \frac{d\widetilde{x}_1}{d\tau} \right) + K_k (\widetilde{x}_2 - \widetilde{x}_1) = K_f - K_g \end{cases} \tag{7}$$

Equation (7) generally interprets a specific class of systems with the same criteria numbers. Therefore, if the equality of the criteria numbers (5) and similarity coefficients (6) is met for the compared models, then these are similar in terms of the selected criteria. Similarity scales corresponding to the accepted reference quantities should be defined when developing a laboratory-scale model similar to a reference object. Then, the similarity scales of the masses s_m, the time s_t and the displacements s_l are introduced:

$$s_m = \frac{M^{mo}}{M^{ob}},\ s_t = \frac{T^{mo}}{T^{ob}},\ s_l = \frac{L^{mo}}{L^{ob}} \tag{8}$$

where designation *ob* refers to the reference object and *mo* to its model. The condition for maintaining the similarity of the model to the object is to meet the equations:

$$K_m^{mo} = K_m^{ob},\ K_b^{mo} = K_b^{ob},\ K_k^{mo} = K_k^{ob},\ K_f^{mo} = K_f^{ob},\ K_g^{mo} = K_g^{ob} \tag{9}$$

Equation (9), supplemented by criteria numbers (5) and similarity scales (8), allows model parameters to be determined in the form as follows:

$$\begin{array}{l} m_2^{mo} = m_2^{ob} s_m,\ b_2^{mo} = b_2^{ob} s_m / s_t,\ k_2^{mo} = k_2^{ob} s_m / s_t^2 \\ m_1^{mo} = m_1^{ob} s_m,\ b_1^{mo} = b_1^{ob} s_m / s_t,\ k_1^{mo} = k_1^{ob} s_m / s_t^2 \end{array} \tag{10}$$

The LM interaction force and the coefficient of the standard gravity can be determined from the formulas:

$$F^{mo} = F^{ob} s_m s_l s_t^{-2},\ g^{mo} = g^{ob} s_l s_t^{-2} \tag{11}$$

The model parameters defined in this way can be used to build a laboratory-scale vibration reduction system of a quarter-vehicle suspension.

2.3. Model Selection

The reference object in this study is the model of a quarter-vehicle suspension belonging to the SUV category. When denoting a reference object with the M1, the model parameters are specified in the first line of Table 1. Since the laboratory model's structure should reflect the object's structure, the model is implemented by the PVRS (see Figure 2). Displacement z is generated by a shaker. The masses m_1 and m_2 and the displacements x_1

and x_2 are mapped by the bearing Plate 1 and Plate 2. Stiffness coefficients k_1 and k_2 are mapped by Springs 1 and Springs 2. Damping coefficients b_1 and b_2 are mapped by viscous friction in the bearings and in the HVRS by the drag forces resulting from the air pumped through the LM.

Table 1. Assumed model parameters.

Model	Coefficient Value	Scaling Factor
M1	$m_2 = 450$ kg, $m_1 = 50$ kg, $b_2 = 1140$ N · s/m, $b_1 = 100$ N · s/m, $k_2 = 20000$ N/m, $k_1 = 128000$ N/m	$s_m = 1$, $s_l = 1$, $s_t = 1$
M2	$m_2 = 12.8$ kg, $m_1 = 1.42$ kg, $b_2 = 32.4$ N · s/m, $b_1 = 2.84$ N · s/m, $k_2 = 568$ N/m, $k_1 = 3635$ N/m	$s_m = 0.0284$, $s_l = 1$, $s_t = 1$
M3	$m_2 = 12.8$ kg, $m_1 = 1.42$ kg, $b_2 = 49.9$ N · s/m, $b_1 = 4.37$ N · s/m, $k_2 = 1347$ N/m, $k_1 = 8617$ N/m	$s_m = 0.0284$, $s_l = 0.1$, $s_t = 0.64935$

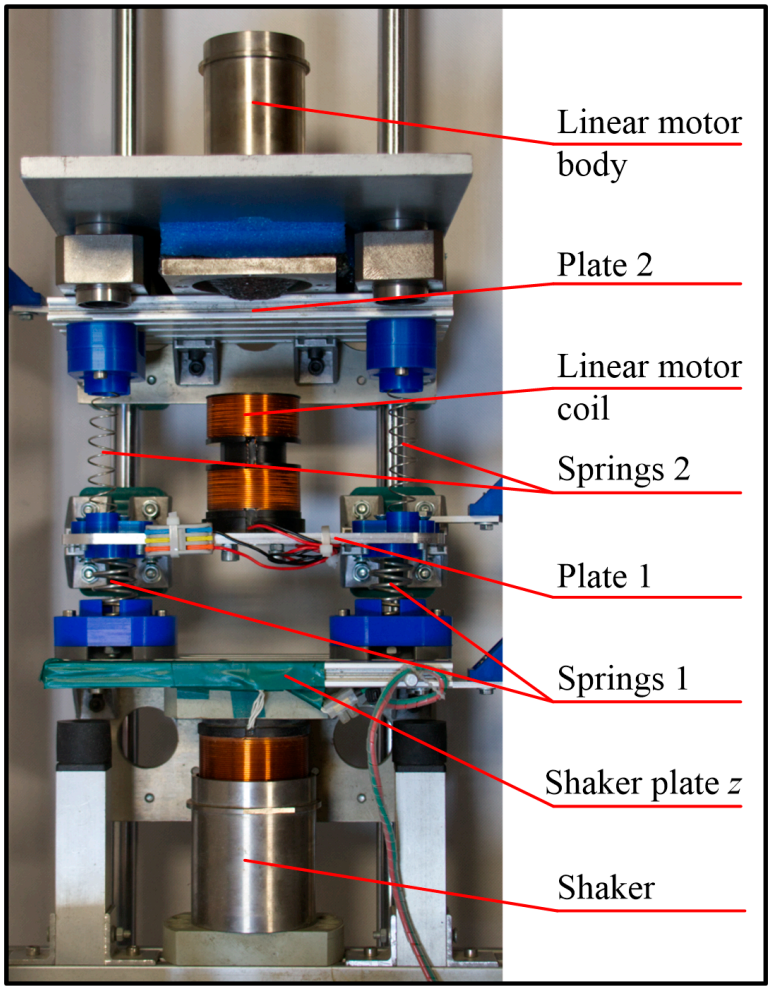

Figure 2. Laboratory implementation of the PVRS.

The primary assumption when choosing the model's parameters is to minimise the amount of energy consumed by the shaker and by the VR, which powers the LM. When analysing Equations (1), (2), (10) and (11), it can be seen that the amount of energy demanded for the functioning of the system increases with the increase of the scale coefficients s_m and s_l and also the decrease of the scale coefficient s_t. However, the effect of the scale

coefficient s_t is not intuitive because the assumption of a value of $s_t < 1$ increases instantaneous energy demand but simultaneously shortens the time required to perform tests. The structure of models usually begins with the assumption $s_l = 1$ and $s_t = 1$, and the coefficient s_m is selected so the model can be made on a laboratory scale (mass, damping, elasticity). The values of the dimensionless similarity coefficients of the reference object are $\alpha_m = 0.111$, $\alpha_b = 0.0877$, $\alpha_k = 6.4$. Taking into account the mass of the bearing arrangements, the sensor, the fasteners, and the LM coil, the mass m_1 cannot be less than 1.42 kg. Knowing the mass m_1, one can estimate the mass $m_2 = 12.8$ kg and the scale factor $s_m = 0.0284$. The remaining parameters are estimated from the relationship (10). The resulting model is marked with the symbol M2 and its coefficients are provided in the second line of Table 1.

The parameters of the M2 indicate that a low damping coefficient b_1 value makes physical implementation difficult, and a low stiffness coefficient k_2 value is unacceptable for safety reasons. In the case of HVRS damage, the Spring 1 could be permanently deformed. An additional limitation is a shaker and an LM's scope of displacements. For these reasons, the M3 was developed, in which the scale factors were modified, assuming $s_l = 0.1$ and $s_t = 0.64935$. The designated coefficients of the model are placed in the third line of Table 1.

When considering mechanical limitations and the availability of springs in the manufacturers' catalogues, a laboratory model of the vibration reduction system designated as M4 was built (see Figure 2). Subsequently, the correctness of the execution of the masses was verified, and the remaining coefficients were identified. The coefficient values of the M4 are provided in the first line of Table 2.

Table 2. Identified model parameters.

Model	Coefficient Value	Electrical Parameter
M4	$m_2 = 12.8$ kg, $m_1 = 1.42$ kg, $b_2 = 35.9$ N · s/m, $b_1 = 3.88$ N · s/m, $k_2 = 1371$ N/m, $k_1 = 7197$ N/m	- ($F_m = 0$ N)
M5	$m_2 = 12.8$ kg, $m_1 = 1.42$ kg, $b_2 = 35.9$ N · s/m, $b_1 = 3.88$ N · s/m, $k_2 = 1371$ N/m, $k_1 = 7197$ N/m	$R_m = 2.4\ \Omega$, $L_m = 2.5$ mH, $R_a = 30.2\ \Omega$, $\kappa_1 = 21.35$ N/A, $\kappa_2 = 21.36$ V · s/m

Comparing the parameters of the M3 and M4, it can be seen that, for elements reproducing the behaviour of the tire (mass m_1), the obtained stiffness and damping coefficients were lower than expected, which resulted in a decrease in the resonant frequency and an increase in vibration amplitude. In the case of the sprung mass (mass m_2), the resonant frequency is mapped correctly, while the amplitude mapping requires increasing the value of the damping factor b_2 by 14 N · s/m. Introduced M1, M2, and M3 described the operation of the PVRS. The implementation of the HVRS requires the activation of the LM, which results in the introduction of additional drag force into the system resulting from air transfer between the core and the motor coil. This force is proportional to the difference $\dot{x_2} - \dot{x_1}$, so it can be modelled as the increment of the damping coefficient b_2. It is also possible to increase the damping coefficient b_2 by including additional resistance R_a in the LM circuit. According to [39], the additional damping value b_d caused by the LM into the suspension system is determined by the formula:

$$b_d = \frac{\kappa_1 \kappa_2}{R_m + R_a} \tag{12}$$

Based on the electrical parameters of the LM (see M5 in Table 2) and the Formula (12), the b_2 value will increase by 14 N · s/m at $R_a = 30.2\ \Omega$. Consideration of the effect of equivalent damping b_d without taking into account drag force resulting from air transfer is only theoretically possible. Despite this, the M5 was introduced in the simulation stage, and its parameters are provided in the second line of Table 2.

3. Numerical Simulations

Simulations were carried out by the LabVIEW Simulation Module Package in two stages. In the first stage, the M2, M3, M4, and M5 were verified, while in the second stage, the HVRS model was developed and tested under deterministic excitation of a step signal, deterministic excitation of a sinusoidally varying signal, and random excitation of a stochastic signal. The sampling time was set to $dt_s = 0.0002$ s.

Deterministic excitation of a step signal was defined as:

$$z(t) = \begin{cases} 0 \text{ m} & \forall \quad t < 1 \cdot s_t \\ 0.001 \cdot s_l & \forall \quad t \geq 1 \cdot s_t \end{cases} \tag{13}$$

In contrast, deterministic excitation of a sinusoidally varying signal was defined as:

$$z(t) = Az \cdot s_l \cdot \sin\left(t^2 / s_t^2 \cdot \pi \cdot v_z\right) \tag{14}$$

where $Az = 1$ mm is a constant amplitude and $v_z = 0.02$ Hz·s^{-1} is the sweep rate at which the frequency f rises from the minimum value to the value of $15/s_t$ Hz. In order to evaluate simulation results, the displacement transmissibility coefficients were introduced:

$$T_{x1z}(f) = \frac{Ax_1}{Az}, \; T_{x2z}(f) = \frac{Ax_2}{Az} \tag{15}$$

where Ax_1 and Ax_2 are the amplitudes of the displacements x_1 and x_2, respectively.

Excitations in the form of a stochastic process are the sum of sinusoidal processes with determined amplitudes and wavenumbers, and the initial phases, being random variables, are defined as:

$$z^{ob}\left(y^{ob}\right) = \sum_{i=1}^{n} A_i \sin\left(k_i y^{ob} + \theta_i\right) \tag{16}$$

The meaning of the markings in the Formula (16) is as follows: n—number of sinusoidal processes, θ_i—random value from the range $< -\pi, \pi)$, y^{ob}—spatial coordinate of the distance covered by the object moving at the speed v_y^{ob}, k_i—wavenumber being a multiple of the minimum wavenumber k_{min}, A_i—amplitude of sinusoidal varying process with the assumed resultant power spectral density (PSD).

Considering the velocity of the reference object $v_y^{ob} = 60$ km/h and the considered vibration frequency in the range from 0.5 Hz to 20 Hz, the wavelength of the y^{ob} coordinate is in the range $(0.83,\ 33.2)$ m for models M1 and M2, and for models M3, M4, and M5, after taking into account $s_t = 0.649$, in the range $(1.3,\ 52)$ m. Considering both intervals, the wavenumbers k_i are in the range $(0.12,\ 7.57)$ rad/m. Analysis of models in the time scale $s_t \neq 1$ or displacement scale $s_l \neq 1$ requires adjustments in the excitation generation process expressed as:

$$z^{mo}(y^{mo}) = s_l \cdot z^{ob}(y^{mo}) \tag{17}$$

where y^{mo} is the spatial coordinate specified for the model moving at $v_y^{mo} = v_y^{ob}/s_t$.

As a result, random excitation was defined as the assembly of three 15-second fragments of stochastic processes representing disturbances occurring on class A, B and C roads under the [55] standard. The component processes $z^{mo}(t^{mo})$ are defined assuming: $k_{min} = 0.05$ rad/m, $n = 220$, $v_y^{ob} = 16.6$ m/s and 3 values of power spectral density: 1.5×10^{-6} m^3/rad, 8×10^{-6} m^3/rad, 3×10^{-5} m^3/rad. The example of a power spectral density of displacement excitation $PSDz^{ob}(k)$ in an A road class is shown in Figure 3.

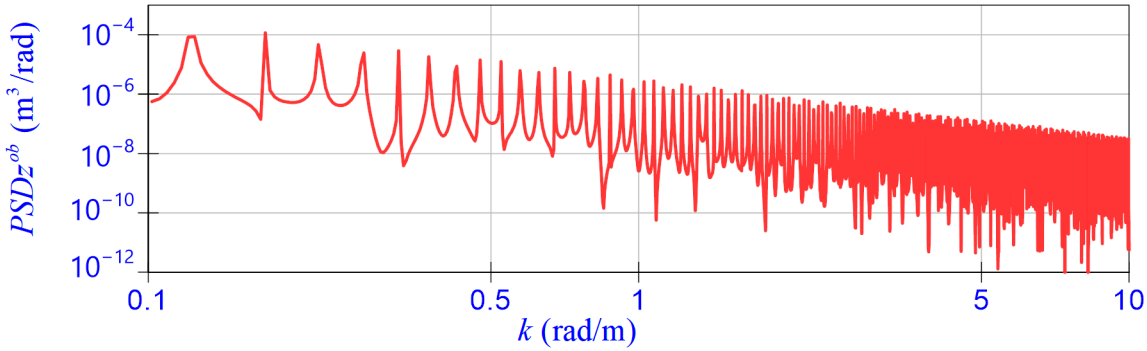

Figure 3. Power spectra density of displacement excitation in an A road class.

3.1. Passive Vibration Reduction System

Verification of the PVRS was carried out under deterministic excitations. To simplify the interpretation of the results, the gravitational interaction was omitted ($g^{ob} = g^{mo} = 0$). Taking into account the influence of the scaling factors s_t and s_l, the sampling time was corrected accordingly, $dt = dt_s/s_t$, and the displacements z, x_1, and x_2 were scaled up. The determined time characteristics are shown in Figure 4 and the displacement transmissibility coefficients in Figure 5.

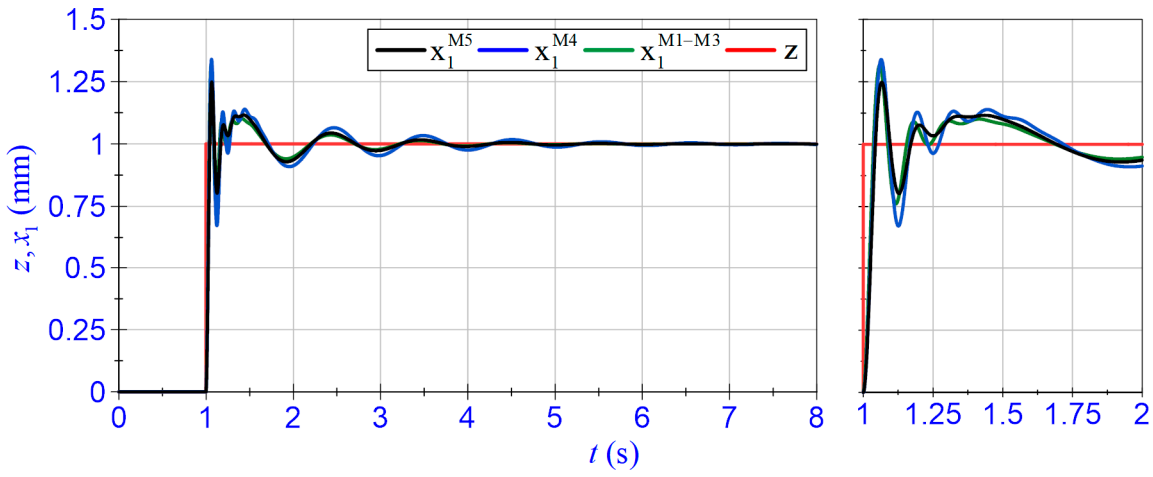

(**a**)

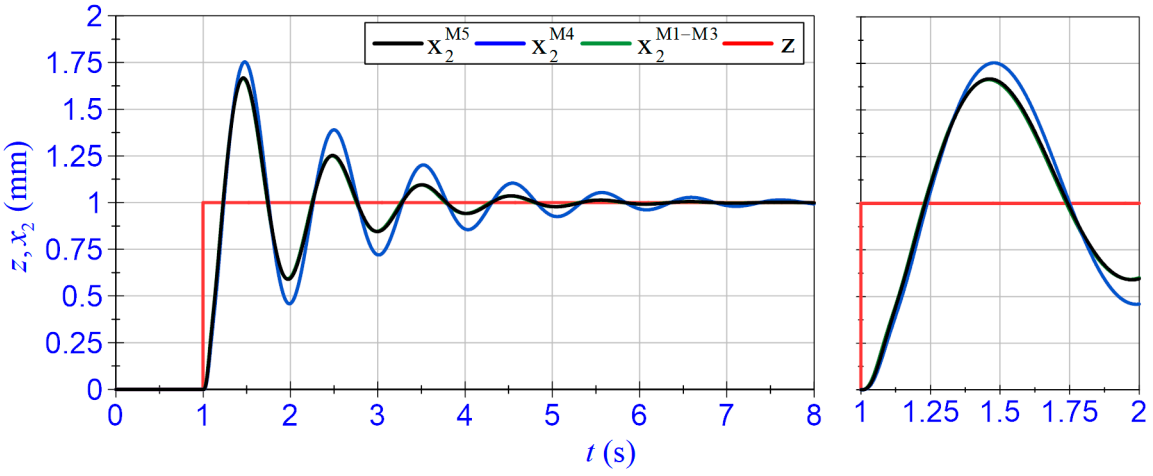

(**b**)

Figure 4. Time patterns: (**a**) displacement z and x_1; (**b**) displacement z and x_2–PVRS.

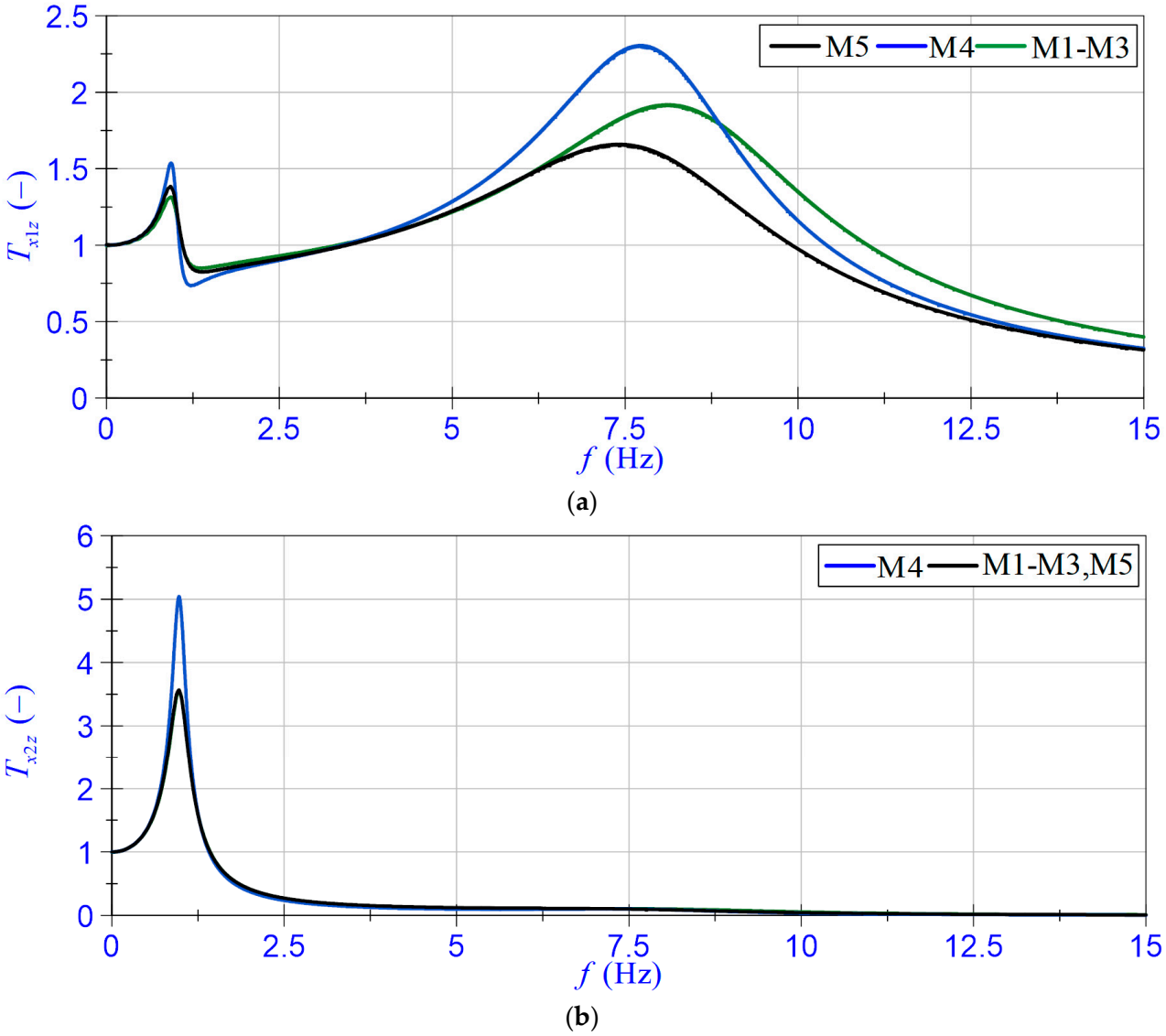

Figure 5. Displacement transmissibility coefficients: (**a**) T_{x1z}; (**b**) T_{x2z}–PVRS.

The analysis of plots in Figures 4 and 5 leads us to the following conclusions:

- The M2 and M3 are similar to the M1;
- Comparison of the M4 and M5 with the M1 shows that in the assumed excitation frequency range, the sprung mass resonant frequency was mapped correctly, while the unsprung mass resonant frequency was lower than expected;
- The M5, in which the damping factor b_2 was increased compared to the M4, accurately reproduces the amplitude of the sprung mass vibrations;
- The transmissibility coefficients T_{x1z} in the high-frequency range for the M5 do not map exactly the transmissibility coefficients T_{x1z} for the M1.

The analysis shows that the similarity of the M1 and M4 is sufficient to verify the possibility of using the HVRS in vehicle suspensions based on calculations carried out in the test rig.

3.2. Hybrid Suspension System

The HVRS requires the development of an LM control module (see Figure 1b), with which the resistance R_a and the supply voltage u_m can be changed. Changing the resistance R_a allows operation in semiactive mode while changing the voltage u_m allows operation in active mode. Given the Formula (12), the effect of the resistance R_a change was simulated

for two boundary values. Using the M5 as the base and assuming $u_m = 0$ V, the M5a for $R_a = 1\ \Omega$ and M5b for $R_a = 50\ \Omega$ were defined. In active mode, the slide mode control algorithm was used to control the HVRS, assuming that the purpose of the control is to minimise the mass m_2 vibrations amplitude. Considering Equations (1) and (2), the motion equation of Plate 2 can be written as:

$$\ddot{x_2} = \frac{1}{m_2} f_d\left(x_1, \dot{x_1}, x_2, \dot{x_2}, t\right) + \frac{1}{m_2} f_c(i_m, t) \tag{18}$$

where f_c is the control force that should counteract the force f_d disturbing the accepted equilibrium point ($x_2 = 0$ and $\dot{x_2} = 0$) [56]. If we assume a sliding variable in the form of $\sigma = \dot{x_2} + cx_2$, then according to [39], a control law u_m can be expressed as:

$$u_m = \frac{m_2 R_m}{\kappa_1} c\dot{x_2} + \frac{R_m}{\kappa_1} \beta \cdot \mathrm{sign}\left(\dot{x_2} + cx_2\right) \tag{19}$$

where c is the angle of the sliding surface on a state trajectory, and β is the parameter chosen to offset the impact of the max value of the disturbing force f_d.

When the system operates in the active mode under deterministic excitations, the amount of energy supplied to the LM in the time duration of 1 s is expressed as:

$$E_{de1} = \frac{\int_{t_n}^{t_{n+1}} \frac{{u_m}^2}{R_m} \cdot \mathrm{d}t}{t_{n+1} - t_n} \tag{20}$$

where $t_{n+1} - t_n$ is the time duration of the one cycle of a sinusoidally varying excitation and n is the cycle number. Whereas the system operates under stochastic excitations, the amount of energy supplied to the LM in the time duration of 1 s can be calculated as:

$$E_{de2} = \int_{t_i}^{t_{i+1}} \frac{{u_m}^2}{R_m} \cdot \mathrm{d}t \tag{21}$$

where t_i is the start time of the cycle, t_{i+1} is the end time, and $t_{i+1} - t_i$ is assumed to be 1 s.

The operation of the vibration reduction system in active mode was implemented using the base M5 and the control law written in the formula (19). Assuming $R_a = 50\ \Omega$, $c = 10\ \mathrm{s}^{-1}$, and 2 values of β = 30 N and 40 N, the M5c and M5d, whose parameters are provided in Table 3, were defined. The M5a–M5c were analysed under sinusoidally varying excitation. The simulation results are shown in Figures 6 and 7. The plots in Figure 6 present the displacement transmissibility coefficients T_{x1z} and T_{x2z} and, in Figure 7, the plot of the energy E_{de1} supplied to the LM as a function of frequency f.

Table 3. Parameters of the semiactive and active model of the system.

Model	β N	c s^{-1}	R_a Ω
M5a	0	0	1
M5b	0	0	50
M5c	30	10	50
M5d	40	10	50

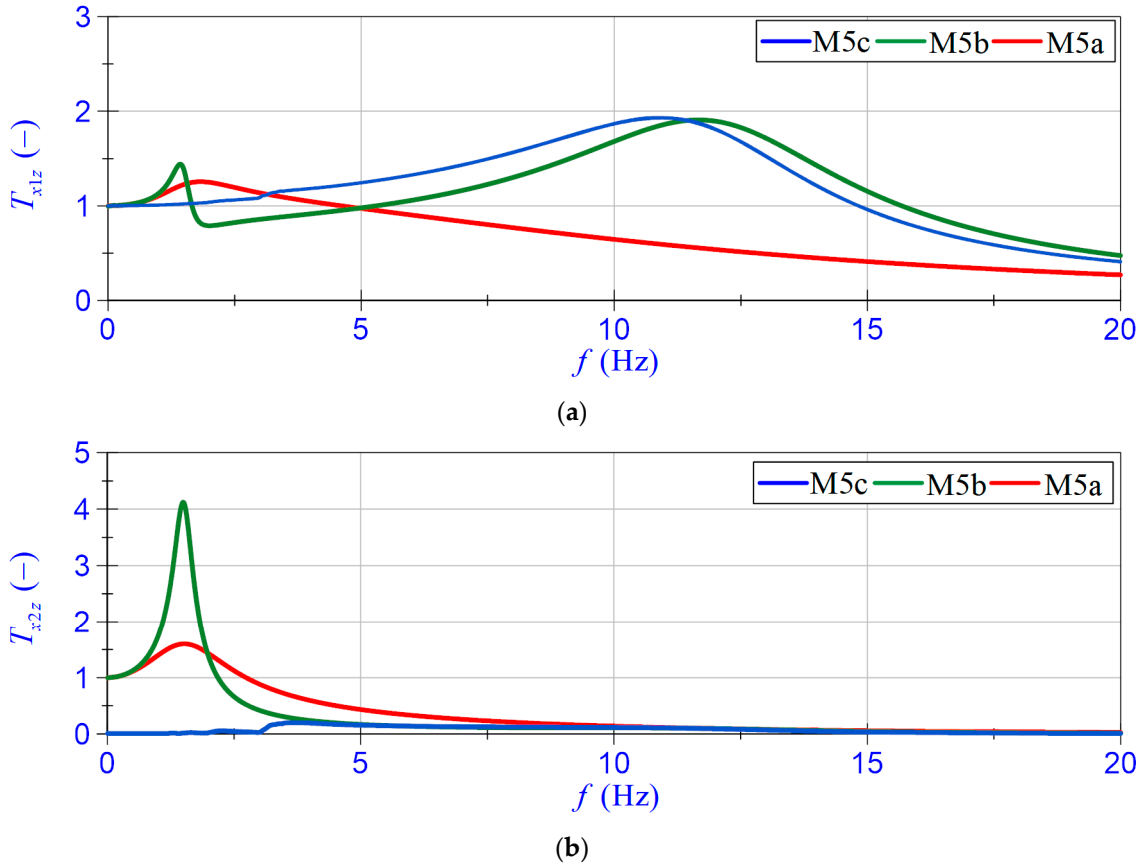

Figure 6. Displacement transmissibility coefficients: (**a**) T_{x1z}; (**b**) T_{x2z}—semiactive and active suspension system.

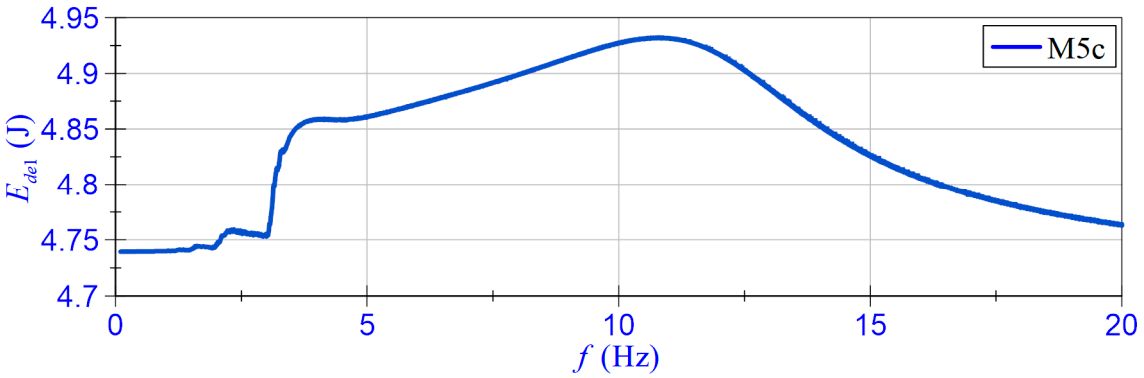

Figure 7. Energy E_{de1} vs. frequency f—active suspension system.

Based on the obtained results, an algorithm for the HVRS control was formulated (see diagram in Figure 8). The algorithm was implemented in three stages: data preparation, determination of excitation type, and model selection. The data preparation stage consisted of the following steps:

- Buffering the last 30,000 displacement z samples;
- Determination $PSDz(f)$ function of the buffered signal;
- Calculation of the maximum value of $PSDz$ designated by PSD^1 and determination of the corresponding frequency designated by f_m^1.

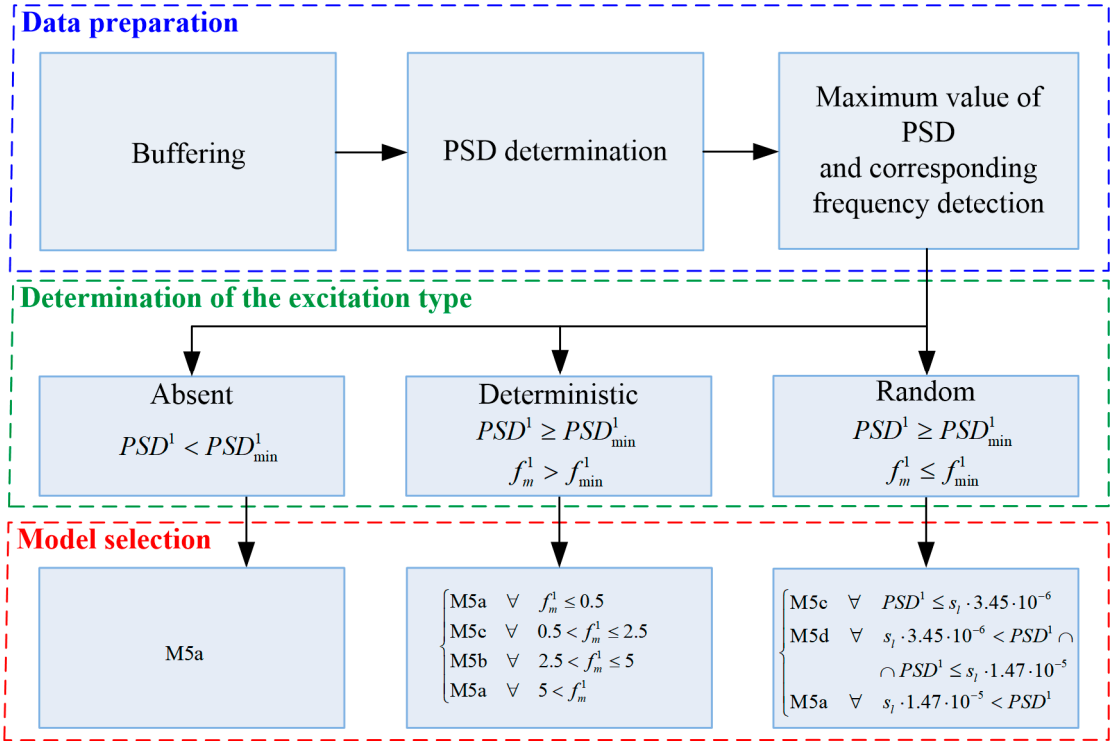

Figure 8. Diagram of the HVRS operation.

The determination of the excitation type stage consists in determining whether there is no excitation or there is deterministic or random excitation. The detection algorithm works by comparing the values PSD^1 and f_m^1 with the experimentally determined limit values $PSD^1_{min} = 10^{-8}\text{m}^2/\text{Hz}$ and $f^1_{min} = 0.25$ Hz. No excitation signal occurs when $PSD^1 < PSD^1_{min}$. If $PSD^1 \geq PSD^1_{min}$ and $f_m^1 > f^1_{min}$, then the excitation is deterministic, and if $PSD^1 \geq PSD^1_{min}$ and $f_m^1 \leq f^1_{min}$, then the excitation is random.

In the last stage, the parameters determining the operation of the vibration reduction system are selected. In the absence of excitation, the HVRS parameters match those of the M5a. The selected parameters of the model allow for energy saving and in the event of short-term excitation, provide a reduction of the amplitude Ax_2. Taking into account the displacement transmissibility coefficients in Figure 6, 3 frequencies, 0.5 Hz, 2.5 Hz, and 5 Hz are defined, for which the values of the HVRS parameters should match the values of the model parameters according to:

$$\text{HVRS parameters} = \begin{cases} \text{M5a} & \forall & f_m^1 \leq 0.5 \\ \text{M5c} & \forall & 0.5 < f_m^1 \leq 2.5 \\ \text{M5b} & \forall & 2.5 < f_m^1 \leq 5 \\ \text{M5a} & \forall & 5 < f_m^1 \end{cases} \tag{22}$$

In the case of random excitations, the choice of model depends on the availability of an external power source. When this source is available, the HVRS should operate in active mode (M5c or M5d). Otherwise, the HVRS should operate in semiactive mode with R_a aiming at 0 Ω (M5a). In active mode, β should be aligned to PSD^1 value, ensuring effective HVRS operation while minimising power consumption. Based on the road's A, B, and C-F class detection, the values of the HVRS parameters were determined under the M5c, M5d, and M5a parameters. The choice of the model parameters occurs according to:

$$\text{HVRS parameters} = \begin{cases} \text{M5c} & \forall & PSD^1 \leq s_l \cdot 3.45 \times 10^{-6} \\ \text{M5d} & \forall & s_l \cdot 3.45 \times 10^{-6} < PSD^1 \leq s_l \cdot 1.47 \times 10^{-5} \\ \text{M5a} & \forall & s_l \cdot 1.47 \times 10^{-5} < PSD^1 \end{cases} \tag{23}$$

The control algorithm was implemented in the model designated as the MH. Then, the model was tested under sinusoidal varying and random excitation, and the results are shown in Figures 9 and 10.

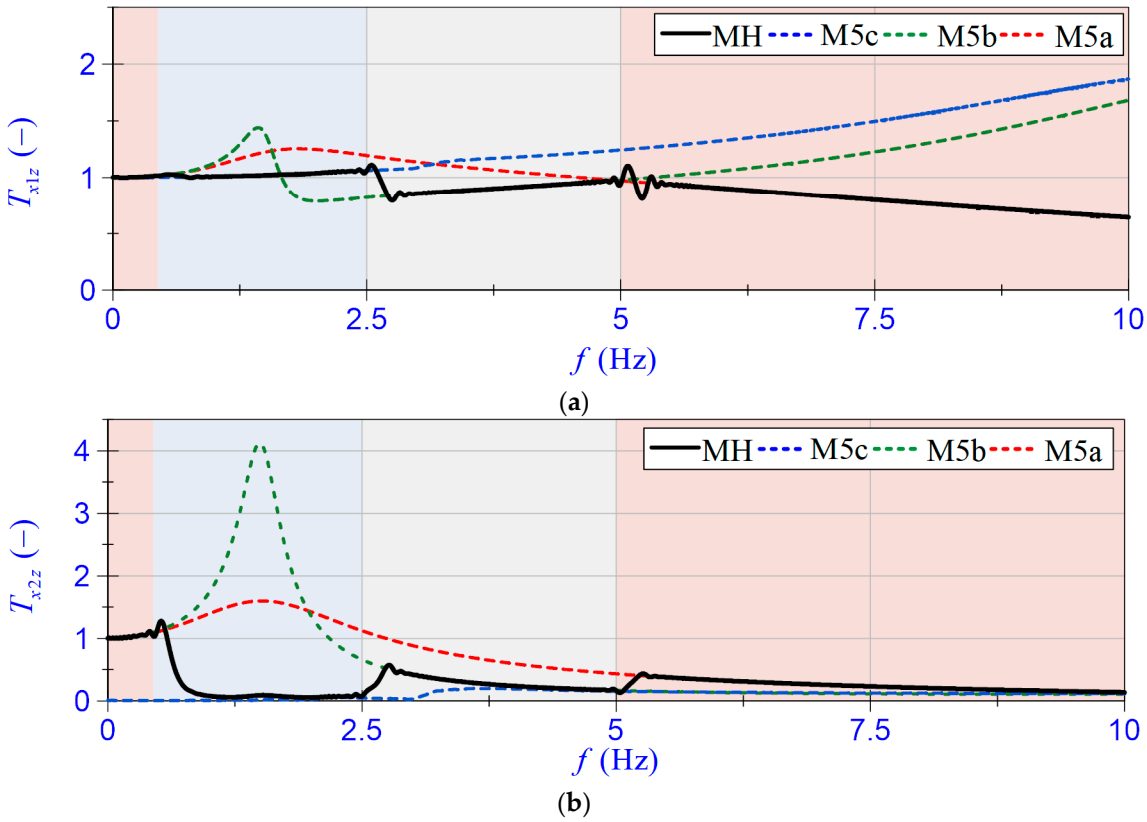

Figure 9. Displacement transmissibility coefficients: (**a**) T_{x1z}; (**b**) T_{x2z}—HVRS.

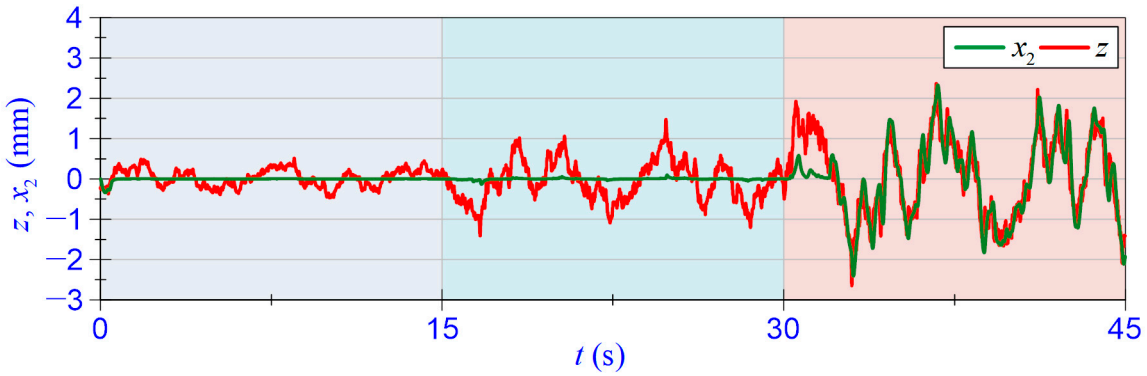

Figure 10. Time patterns of displacement z and x_2—HVRS.

The simulation results revealed that the algorithm proposed for detecting the type of excitation operates appropriately. Regardless of the excitation, the algorithm shows around 3 s delay time, the value of which depends on the number of buffered samples. With deterministic excitation, the algorithm works so that in the low frequency range it provides a reduction of vibration amplitude Ax_2. In the high-frequency range, the algorithm does not cause an increase of vibration amplitude Ax_1. In the case of random excitation, the operation of HVRS in active mode is effective. At the same time, in semiactive mode, the standard deviation x_2 does not exceed the standard deviation z.

4. Experiments

Since the simulation results showed that the HVRS improves the operating conditions of the suspension, experimental verification of the algorithm operation was carried out using the physical model (see Figure 8).

4.1. Hardware

Experiments were conducted in the test rig shown in Figure 11. The stand consists of an aluminium frame to which a shaker (linear electrodynamic motor) generating displacement z of its plate is attached. The shaker plate is connected to Plate 1 and Plate 2 using the Springs 1 and Springs 2 sets. The displacement x_1 is carried out by Plate 1 and the displacement x_2 by Plate 2. Between Plate 1 and Plate 2, there is an LM series of LA25 [57]. Other elements of the test rig are: a set of power supplies, three linear encoders (Sensor 1 [58], Sensor 2 [58], and Sensor 3 [59]), an industrial cRIO 9063 controller [60], a controlled potentiometer, and a PC.

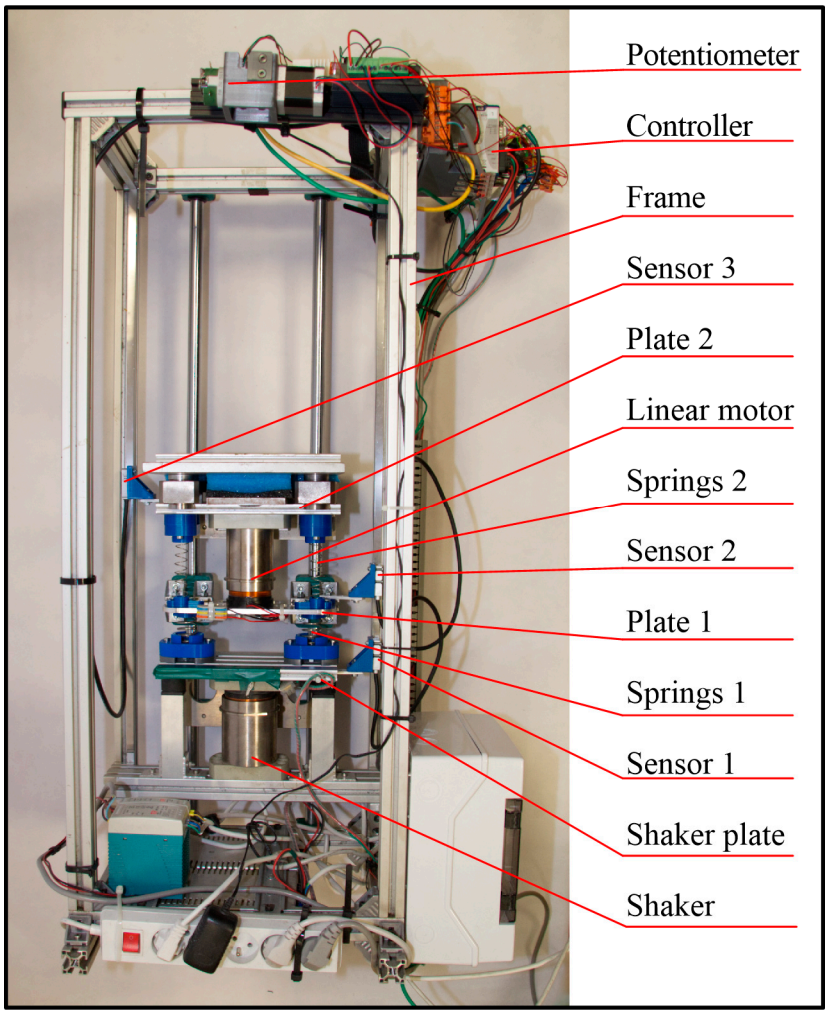

Figure 11. Test rig.

The cRIO-9063 is a hybrid controller enabling hardware implementation of control algorithms on the FPGA module and software in the Real-Time Linux environment implemented by the RT processor. The control modules (inputs, outputs) are connected to a four-port communication bus (chassis). The following modules were used in the experiments:

- NI-9505 for generating shaker plate displacement z and acquisition of a displacement z with Sensor 1;
- NI-9505 for generating voltage u_m realised by VR and acquisition of a displacement x_1 with Sensor 2;
- NI 9401 digital inputs and outputs for control of a potentiometer R_a;
- NI-9215 for displacement x_2 acquisition with Sensor 3.

4.2. Implementation Methods

The implemented HVRS control algorithm and the vibration excitation generating algorithm consists of two parts, implemented in hardware and software. A direct control layer implemented by the FPGA module and a supervisory control layer implemented in RT Linux on the cRIO controller and in Windows on the PC are distinguished. The following algorithms are implemented in the direct control layer: data acquisition, slide mode control, potentiometer control, generation of deterministic or random excitations, and support for safety functions. In the supervisory control layer, the algorithms responsible for detecting the excitation signal, selecting model parameters, and archiving the measurement data are implemented. On the other hand, Windows is used to implement the control panel. The block diagram of the control system developed for the HVRS is shown in Figure 12.

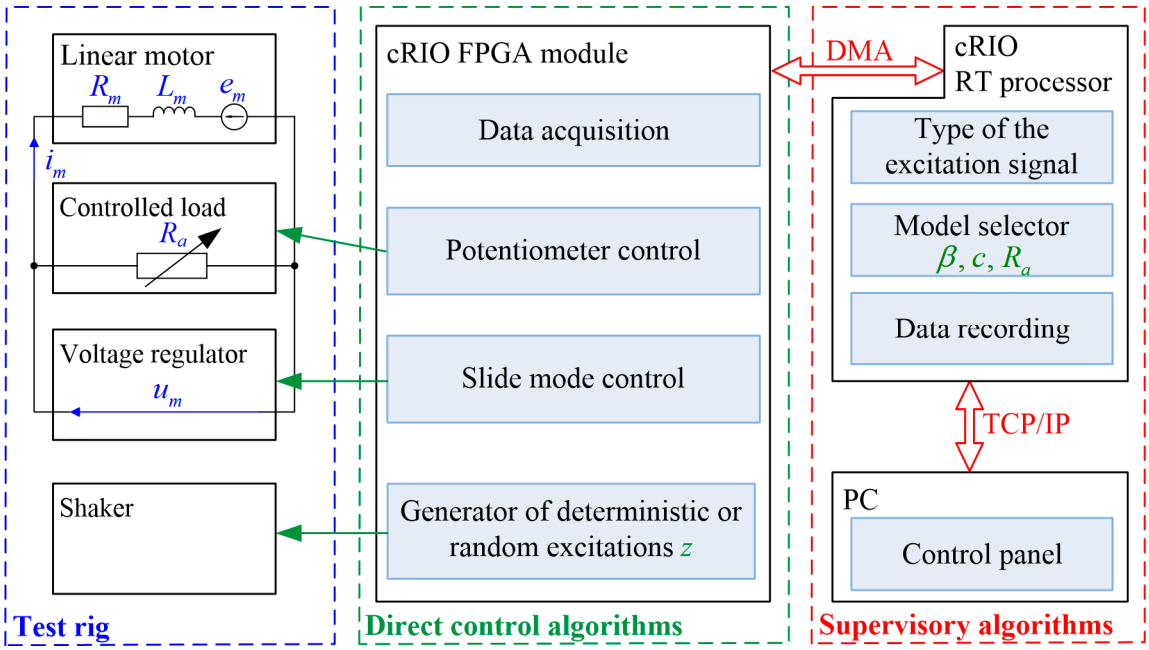

Figure 12. Block diagram of the control system—HVRS.

The tests of HVRS were conducted with a sampling frequency of 4 kHz for algorithms implemented by the FPGA module and 0.1 kHz for algorithms implemented in the RT system. The HVRS response was recorded with sinusoidal varying and random excitation z. The parameters of the sinusoidally varying excitation were $A_z = 0.8$ mm and f from 0.15 Hz to 10 Hz with a sweep rate 0.02 Hz·s^{-1} (the time duration of the cycle was equal to 492 s). The random excitation was achieved according to the Formulas (16) and (17), as in numerical simulations. The LM parameters used in the experiment were identical to those in the simulation (see Table 2).

4.3. Results and Discussion

The M4 was developed for a test rig mapping the PVRS in which it was assumed that the masses m_1 and m_2 take into account the mass of the LM. Therefore, running the HVRS increases only the parameter b_2 value. The parameters $PSD_{min} = 10^{-7}\text{m}^2/\text{Hz}$ and

$f^1_{min} = 0.25$ Hz of the algorithm were selected by analysing the operation of the vibration reduction system for: $R_a = 1\ \Omega$ (model MS1), $R_a = 25\ \Omega$ (model MS2), $\beta = 20$ N and $c = 10\ \mathrm{s}^{-1}$ (model MA1), and $\beta = 30$ N and $c = 10\ \mathrm{s}^{-1}$ (model MA2). As can be seen, in the MS1 and MS2, the value of the R_a parameter was reduced in relation to the parameters of the M5. The modification was performed to compensate for the increase in the parameter b_2. Additional delays and measurement inaccuracies resulting from signal processing by Sensor 3 cause an increase in the chattering effect. This is manifested by high-frequency vibrations [61] and can be reduced by modifying the value of the β parameter or using additional anti-chattering filters. To maintain experimental results, the MA1 and MA2 have reduced β by 10 N compared to M5C and M5d. The strategy of the HVRS under deterministic excitations results from the analysis of the displacement transmissibility coefficients T_{x1z}, T_{x2z} and considers the energy consumption of the LM only in active mode. Whereas the strategy of the HVRS under stochastic excitations is to adjust the value of parameter β to the road class or to switch the system to semiactive mode with a minimal value of R_a. In the case of the MA1, the value of parameter β has been selected to be fully sufficient for class A roads, not necessarily sufficient for class B roads, and certainly not sufficient for class C roads. In the case of the MA2, similar assumptions have been made, increasing the class of the road by one. The chosen coefficients of the control algorithm for the HVRS are provided in Table 4 (model MH1). The size of the buffer required to correctly determine the coefficients PSD^1 and f^1_m was set at 30,000 samples.

Table 4. Parameters of the proposed control algorithm.

Semiactive or Active Control Algorithm	**β N**	**$c\ \mathrm{s}^{-1}$**	**$R_a\ \Omega$**
MS1	0	0	1
MS2	0	0	25
MA1	20	10	25
MA2	30	10	25
Hybrid control algorithm MH1			
Type of signal	Ranges	Type of model	
absent	-	MS1	
Deterministic	$f^1_m \le 0.5$	MS1	
	$0.5 < f^1_m \le 2.4$	MA1	
	$2.4 < f^1_m \le 4.8$	MS2	
	$4.8 < f^1_m$	MS1	
Random	$PSD^1 \le s_l \cdot 3.45 \times 10^{-6}$	MA1	
	$s_l \cdot 3.45 \times 10^{-6} < PSD^1 \le s_l \cdot 1.47 \times 10^{-5}$	MA2	
	$s_l \cdot 1.47 \times 10^{-5} < PSD^1$	MS1	

The plots of displacement transmissibility coefficients T_{x1z} and T_{x2z} are shown in Figure 13. Comparing experimental and simulation results, it can be concluded that under deterministic excitation, the HVRS operates correctly (see Figure 9). The differences between the M5a and MS1 and the M5b and MS2 are due to not considering static friction and drag forces resulting from the air pumped through the LM. When comparing the M5c and MA1 for the frequency $f < 6$ Hz in the MA1, one can see the increase in the coefficients T_{x1z} and T_{x2z} caused by the chattering effect. For the frequency $f \ge 6$ Hz in the MA1, the value of the parameter $\beta = 20$ N is too small to compensate for the disturbing forces, so the values of the coefficients T_{x1z} and T_{x2z} increase.

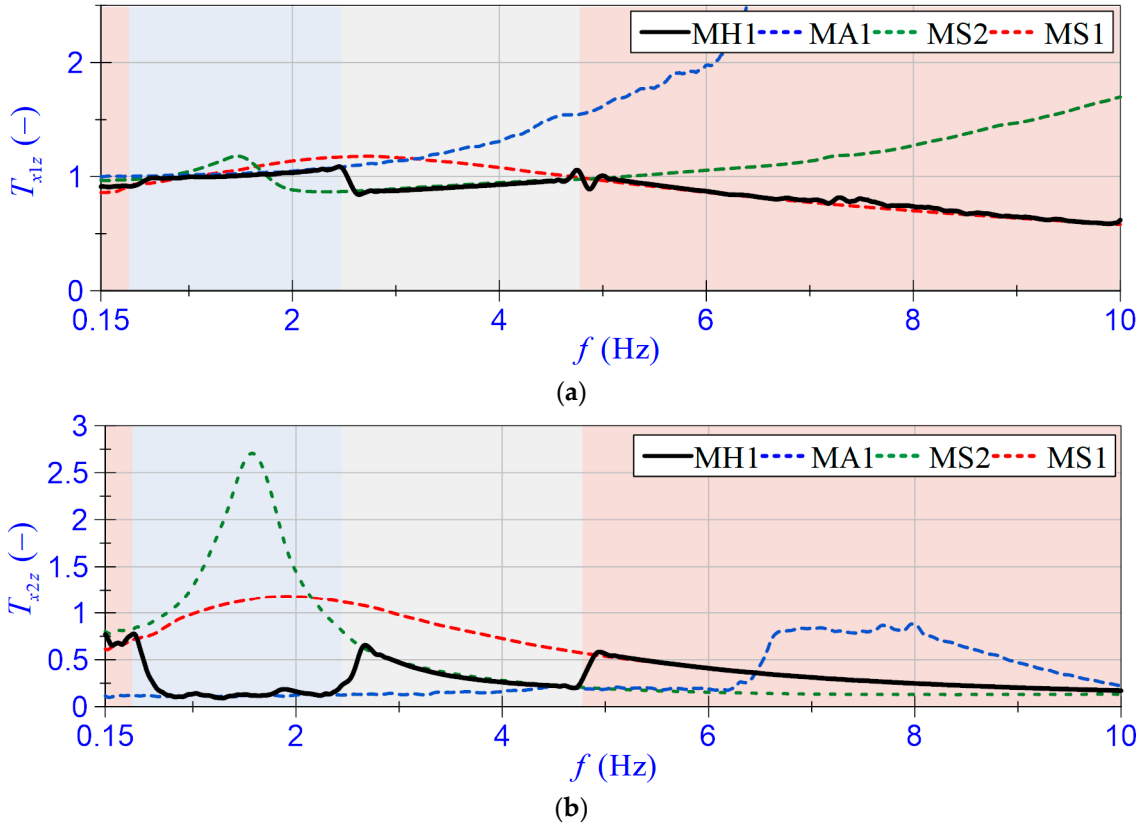

Figure 13. Displacement transmissibility coefficients: (**a**) T_{x1z}; (**b**) T_{x2z}—experiments.

The HVRS response to random excitation is illustrated in Figure 14. It can be seen that the control algorithm detects the type of excitation and the road class properly. The system's reaction time to a change of road class does not exceed 3 s. The effectiveness of the HVRS depends on the adopted value of the β parameter, so the use of the MA2 parameters for a class A road causes an increase in the standard deviation x_2 and results in unnecessary energy wastage. Therefore, using the parameters of the MA1 on a class B road or the parameters of the MA2 on a class C road can mostly be sufficient, but leaves no margin for error in the case of an increase in the value of PSD^1.

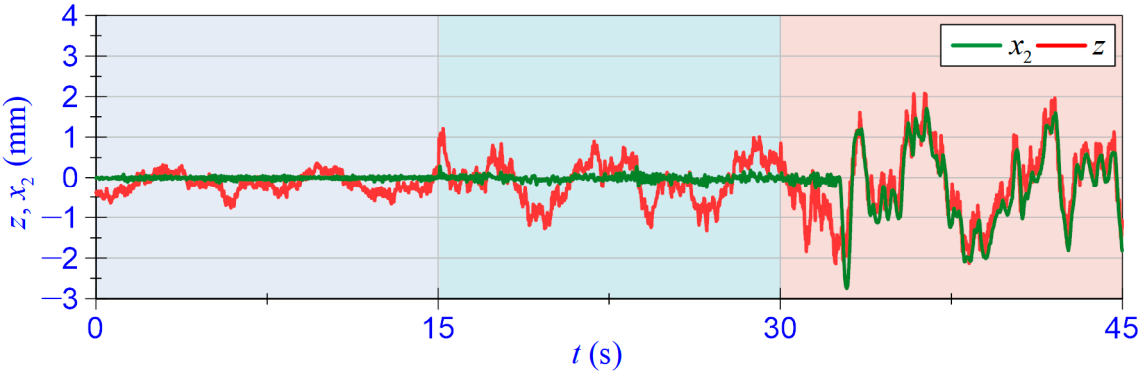

Figure 14. Time patterns of displacement z and x_2—experiments.

5. Summary

The study investigates the HVRS equipped with the LM under deterministic and random excitations. The simulation and experimental results lead the authors to the following conclusions:

- The method of dynamic similarity allows obtaining satisfactory accuracy in mapping the dynamics of the reference object by a scaled vibration reduction system.
- Correct reference of test results conducted for models with scaling factors $s_m \neq 1$, $s_l \neq 1$, or $s_t \neq 1$ with respect to the reference object requires scaling both the measured output values and generated excitation.
- The random excitations allow mapping of the surface roughness for roads in class A–C and consider the scaling time and displacement factors.
- An important advantage of the described scaling method is reducing the test rig building cost. The energy saving in the research stage is significant and can be proven by considering Formulas (2) and (11). The product of $s_m s_l s_t^{-2}$ is equal to 0.00673, so the forces generated by the LM and shaker in the test rig are about 148 less than the forces which should be generated in a full-scale model. Neglecting the restrictions in the selection of the LM and assuming $\kappa_1^{mo} = \kappa_1^{ob}$, the value of i_m should be significantly larger in a full-scale model. In addition, the value of the scaling factor $s_t = 0.649$ shortens the time required to perform experiments.
- Regardless of the adopted scaling factors, the power saving achieved during the HVRS operation results from the amount of energy supplied to the LM. Under deterministic excitations, the LM is supplied only in a narrow frequency range (active mode), and under stochastic excitation, the value of parameter β is adjusted to the road class, or the system is switched to semiactive mode with a minimal value of R_a. According to the former study [50], the amount of energy consumed by the LM increases with the increase in the β parameter value.
- The effectiveness of the HVRS is much greater than that of the PVRS, regardless of the type of excitation.
- The effectiveness of the HVRS for deterministic excitations depends on the frequency f. The results of numerical simulations in the considered frequency range from 0.8 Hz to 10 Hz showed that the value of the coefficient T_{x2z} (sprung mass) does not exceed 0.57 and the value of the coefficient T_{x1z} does not exceed 1.11 (unsprung mass).
- The tests performed showed that the proposed algorithm for detecting the excitation signal works properly regardless of whether the displacement z or the difference in displacement $x_1 - x_2$ is used as a feedback signal.
- The assumption of a large number of buffered samples in the data preparation step introduces about a 3 s delay in excitation detection. This delay has a positive effect because it prevents the frequent switching of the R_a, β, and c values.
- In the practical implementation of the HVRS, the PSD^1_{min} value may be assumed by measuring the maximum instantaneous value of PSD^1 for the vibration reduction system with no excitation and setting PSD^1_{min} to a slightly higher value. Meanwhile, the value of f^1_{min} should also be slightly higher than the resolution value in the frequency scale used in the PSD function calculation.

Further research will be focused on the development of low-power control electronics, the implementation of anti-chattering filters to improve HVRS performance, and the robustness analysis.

Author Contributions: Conceptualisation, B.S. and P.O.; validation of measurement sensors, P.O.; software implementation for the measurement and control systems, P.O.; planned and carried out experiments, B.S. and P.O.; processed data, B.S. and P.O.; data validation P.O.; supervision, B.S. All authors have read and agreed to the published version of the manuscript.

Funding: This research was funded by the AGH University of Science and Technology within the scope of the research program No. 16.16.130.942 and Excellence Initiative—Research University.

Data Availability Statement: Experimental data may be available with the agreement of the AGH University of Science and Technology.

Conflicts of Interest: The authors declare no conflict of interest.

References

1. Rajamani, R. *Vehicle Dynamics and Control*; Springer Science & Business Media: Berlin/Heidelberg, Germany, 2011.
2. Gillespie, T. *Fundamentals of Vehicle Dynamics*; SAE International: Warrendale, PA, USA, 2021; ISBN 978-1-4686-0177-0.
3. Pauwelussen, J. *Essentials of Vehicle Dynamics*; Butterworth-Heinemann: Oxford, UK, 2014; ISBN 978-0-08-100058-8.
4. Heidarian, A.; Wang, X. Review on Seat Suspension System Technology Development. *Appl. Sci.* **2019**, *9*, 2834. [CrossRef]
5. Tu, L.; Ning, D.; Sun, S.; Li, W.; Huang, H.; Dong, M.; Du, H. A Novel Negative Stiffness Magnetic Spring Design for Vehicle Seat Suspension System. *Mechatronics* **2020**, *68*, 102370. [CrossRef]
6. Babusiak, B.; Hajducik, A.; Medvecky, S.; Lukac, M.; Klarak, J. Design of Smart Steering Wheel for Unobtrusive Health and Drowsiness Monitoring. *Sensors* **2021**, *21*, 5285. [CrossRef]
7. Kari, M.; Grosse-Puppendahl, T.; Jagaciak, A.; Bethge, D.; Schütte, R.; Holz, C. SoundsRide: Affordance-Synchronized Music Mixing for In-Car Audio Augmented Reality. In Proceedings of the 34th Annual ACM Symposium on User Interface Software and Technology, Virtual Event, 10–14 October 2021; pp. 118–133.
8. Matviienko, A.; Löcken, A.; El Ali, A.; Heuten, W.; Boll, S. NaviLight: Investigating Ambient Light Displays for Turn-by-Turn Navigation in Cars. In Proceedings of the 18th International Conference on Human-Computer Interaction with Mobile Devices and Services, Florence, Italy, 6–9 September 2016; pp. 283–294.
9. Gao, Z.; Wang, J.; Wang, D. Dynamic Modeling and Steering Performance Analysis of Active Front Steering System. *Procedia Eng.* **2011**, *15*, 1030–1035. [CrossRef]
10. Reda, A.; Bouzid, A.; Vásárhelyi, J. Model Predictive Control for Automated Vehicle Steering. *Acta Polytech. Hung.* **2020**, *17*, 163–182. [CrossRef]
11. Wei, C.; Wang, Y.; Asakura, Y.; Ma, L. A Nonlinear Programing Model for Collision-Free Lane-Change Trajectory Planning Based on Vehicle-to-Vehicle Communication. *J. Transp. Saf. Secur.* **2021**, *13*, 936–956. [CrossRef]
12. Arcoumanis, C. *Internal Combustion Engines*; Elsevier: Amsterdam, The Netherlands, 2012; ISBN 978-0-323-15179-5.
13. Hamid, A.F.A.; Rahman, M.T.A.; Khan, S.F.; Adom, A.H.; Rahim, M.A.; Rahim, N.A.; Ismail, M.H.N.; Norizan, A. Connected Car: Engines Diagnostic via Internet of Things (IoT). *J. Phys. Conf. Ser.* **2017**, *908*, 012079. [CrossRef]
14. Benajes, J.; García, A.; Pastor, J.M.; Monsalve-Serrano, J. Effects of Piston Bowl Geometry on Reactivity Controlled Compression Ignition Heat Transfer and Combustion Losses at Different Engine Loads. *Energy* **2016**, *98*, 64–77. [CrossRef]
15. Holmberg, K.; Andersson, P.; Erdemir, A. Global Energy Consumption Due to Friction in Passenger Cars. *Tribol. Int.* **2012**, *47*, 221–234. [CrossRef]
16. Wu, J.; Zhang, H.; He, R.; Chen, P.; Chen, H. A Mechatronic Brake Booster for Electric Vehicles: Design, Control, and Experiment. *IEEE Trans. Veh. Technol.* **2020**, *69*, 7040–7053. [CrossRef]
17. Deo, A.; Palade, V.; Huda, M.N. Centralised and Decentralised Sensor Fusion-Based Emergency Brake Assist. *Sensors* **2021**, *21*, 5422. [CrossRef] [PubMed]
18. Belhocine, A.; Afzal, A. Computational Finite Element Analysis of Brake Disc Rotors Employing Different Materials. *Aust. J. Mech. Eng.* **2022**, *20*, 637–650. [CrossRef]
19. Schnelle, S.; Wang, J.; Jagacinski, R.; Su, H. A Feedforward and Feedback Integrated Lateral and Longitudinal Driver Model for Personalized Advanced Driver Assistance Systems. *Mechatronics* **2018**, *50*, 177–188. [CrossRef]
20. Sun, S.; Petropulu, A.P.; Poor, H.V. MIMO Radar for Advanced Driver-Assistance Systems and Autonomous Driving: Advantages and Challenges. *IEEE Signal Process. Mag.* **2020**, *37*, 98–117. [CrossRef]
21. Stojanovic, N.; Abdullah, O.I.; Grujic, I.; Glisovic, J.; Belhocine, A. The Influence of Spoiler on the Aerodynamic Performances and Longitudinal Stability of the Passenger Car under High Speed Condition. *J. Vis.* **2022**, *26*, 97–112. [CrossRef]
22. Aljarbouh, A.; Fayaz, M.; Qureshi, M.S.; Boujoudar, Y. Hybrid Sliding Mode Control of Full-Car Semi-Active Suspension Systems. *Symmetry* **2021**, *13*, 2442. [CrossRef]
23. Krtolica, R.; Hrovat, D. Optimal Active Suspension Control Based on a Half-Car Model. In Proceedings of the 29th IEEE Conference on Decision and Control, Honolulu, HI, USA, 5–7 December 1990; 1990; Volume 4, pp. 2238–2243.
24. Prabakar, R.S.; Sujatha, C.; Narayanan, S. Optimal Semi-Active Preview Control Response of a Half Car Vehicle Model with Magnetorheological Damper. *J. Sound Vib.* **2009**, *326*, 400–420. [CrossRef]
25. Munawwarah, S.; Yakub, F. Control Analysis of Vehicle Ride Comfort through Integrated Control Devices on the Quarter and Half Car Active Suspension Systems. *Proc. Inst. Mech. Eng. Part D J. Automob. Eng.* **2021**, *235*, 1256–1268. [CrossRef]
26. Laalej, H.; Lang, Z.Q.; Sapinski, B.; Martynowicz, P. MR Damper Based Implementation of Nonlinear Damping for a Pitch Plane Suspension System. *Smart Mater. Struct.* **2012**, *21*, 045006. [CrossRef]
27. Konieczny, J.; Sibielak, M.; Rączka, W. Active Vehicle Suspension with Anti-Roll System Based on Advanced Sliding Mode Controller. *Energies* **2020**, *13*, 5560. [CrossRef]
28. Naveen, A. Isuzu D-Max—Offering New Technology in The LCV Space. *Auto Tech. Rev.* **2014**, *3*, 50–51. [CrossRef]
29. Lozia, Z.; Zdanowicz, P. Optimization of Damping in the Passive Automotive Suspension System with Using Two Quarter-Car Models. *IOP Conf. Ser. Mater. Sci. Eng.* **2016**, *148*, 012014. [CrossRef]
30. Gobbi, M.; Levi, F.; Mastinu, G. Multi-Objective Stochastic Optimisation of the Suspension System of Road Vehicles. *J. Sound Vib.* **2006**, *298*, 1055–1072. [CrossRef]

31. Negash, B.A.; You, W.; Lee, J.; Lee, C.; Lee, K. Semi-Active Control of a Nonlinear Quarter-Car Model of Hyperloop Capsule Vehicle with Skyhook and Mixed Skyhook-Acceleration Driven Damper Controller. *Adv. Mech. Eng.* **2021**, *13*, 168781402199952. [CrossRef]
32. Skotnikov, G.I.; Jileykin, M.M.; Komissarov, A.I. Increasing the Stability of the Articulated Lorry at Braking by Locking the Fifth Wheel Coupling. *IOP Conf. Ser. Mater. Sci. Eng.* **2018**, *315*, 012027. [CrossRef]
33. Snamina, J.; Orkisz, P. Energy Harvesting from Vibrations of a Two-Degree-of-Freedom Mechanical System. *Acta Phys. Pol. A* **2014**, 125. [CrossRef]
34. Kashem, S.; Nagarajah, R.; Ektesabi, M. (Eds.) Vehicle Suspension System. In *Vehicle Suspension Systems and Electromagnetic Dampers*; Springer Tracts in Mechanical Engineering; Springer: Singapore, 2018; pp. 23–37. ISBN 978-981-10-5478-5.
35. Strecker, Z.; Mazůrek, I.; Roupec, J.; Klapka, M. Influence of MR Damper Response Time on Semiactive Suspension Control Efficiency. *Meccanica* **2015**, *50*, 1949–1959. [CrossRef]
36. Ho, C.; Lang, Z.Q.; Sapiński, B.; Billings, S.A. Vibration Isolation Using Nonlinear Damping Implemented by a Feedback-Controlled MR Damper. *Smart Mater. Struct.* **2013**, *22*, 105010. [CrossRef]
37. Koch, G.; Kloiber, T. Driving State Adaptive Control of an Active Vehicle Suspension System. *IEEE Trans. Contr. Syst. Technol.* **2014**, *22*, 44–57. [CrossRef]
38. Gysen, B.L.J.; Paulides, J.J.H.; Janssen, J.L.G.; Lomonova, E.A. Active Electromagnetic Suspension System for Improved Vehicle Dynamics. *IEEE Trans. Veh. Technol.* **2010**, *59*, 1156–1163. [CrossRef]
39. Orkisz, P.; Sapiński, B. Vibration Reduction System with a Linear Motor: Operation Modes, Dynamic Performance, Energy Consumption. *Energies* **2022**, *15*, 1910. [CrossRef]
40. Shi, D.; Chen, L.; Wang, R.; Jiang, H.; Shen, Y. Design and Experiment Study of a Semi-Active Energy-Regenerative Suspension System. *Smart Mater. Struct.* **2015**, *24*, 015001. [CrossRef]
41. Moaaz, A.O.; Ghazaly, N.M. Fuzzy and PID Controlled Active Suspension System and Passive Suspension System Comparison. *Int. J. Adv. Sci. Technol.* **2019**, *28*, 1721–1729.
42. Ebrahimi, B.; Bolandhemmat, H.; Khamesee, M.B.; Golnaraghi, F. A Hybrid Electromagnetic Shock Absorber for Active Vehicle Suspension Systems. *Veh. Syst. Dyn.* **2011**, *49*, 311–332. [CrossRef]
43. Patra, A.K. Backstepping LQG Controller Design for Stabilizing and Trajectory Tracking of Vehicle Suspension System. *SN Appl. Sci.* **2020**, *2*, 190. [CrossRef]
44. Qin, W.; Shangguan, W.-B.; Xu, P.; Feng, H.; Sun, Y. *A Study on Sliding Mode Control for Active Suspension System*; SAE Technical Paper 2020-01-1084; SAE International: Warrendale, PA, USA, 2020.
45. Li, M.; Zhang, Y.; Geng, Y. Fault-Tolerant Sliding Mode Control for Uncertain Active Suspension Systems against Simultaneous Actuator and Sensor Faults via a Novel Sliding Mode Observer. *Optim. Control. Appl. Methods* **2018**, *39*, 1728–1749. [CrossRef]
46. Drehmer, L.R.C.; Paucar Casas, W.J.; Gomes, H.M. Parameters Optimisation of a Vehicle Suspension System Using a Particle Swarm Optimisation Algorithm. *Veh. Syst. Dyn.* **2015**, *53*, 449–474. [CrossRef]
47. Dutta, S.; Choi, S.-M.; Choi, S.-B. A New Adaptive Sliding Mode Control for Macpherson Strut Suspension System with Magneto-Rheological Damper. *J. Intell. Mater. Syst. Struct.* **2016**, *27*, 2795–2809. [CrossRef]
48. Sun, X.; Cai, Y.; Yuan, C.; Chen, L.; Wang, R. Hybrid Model Predictive Control of Damping Multi-Mode Switching Damper for Vehicle Suspensions. *J. Vibroengineering* **2017**, *19*, 2910–2930. [CrossRef]
49. Ding, R.; Wang, R.; Meng, X.; Chen, L. Energy Consumption Sensitivity Analysis and Energy-Reduction Control of Hybrid Electromagnetic Active Suspension. *Mech. Syst. Signal Process.* **2019**, *134*, 106301. [CrossRef]
50. Snamina, J.; Orkisz, P. Active Vibration Reduction System with Mass Damper Tuned Using the Sliding Mode Control Algorithm. *J. Low Freq. Noise Vib. Act. Control.* **2021**, *40*, 540–554. [CrossRef]
51. Xie, L.; Li, J.; Cai, S.; Li, X. Electromagnetic Energy-Harvesting Damper With Multiple Independently Controlled Transducers: On-Demand Damping and Optimal Energy Regeneration. *IEEE/ASME Trans. Mechatron.* **2017**, *22*, 2705–2713. [CrossRef]
52. Korzeniowski, R.; Kowal, J.; Pluta, J. Modelling, Simulations and Experimental Investigation of a Hybrid, Electrofluid Vehicle Suspension. *Arch. Control. Sci.* **2005**, *15*, 217.
53. Bolster, D.; Hershberger, R.E.; Donnelly, R.J. Dynamic Similarity, the Dimensionless Science. *Phys. Today* **2011**, *64*, 42–47. [CrossRef]
54. Sedov, L.I. Similarity, Modelling and Various Examples of the Application of Dimensional Analysis. In *Similarity and Dimensional Methods in Mechanics*; Elsevier: Amsterdam, The Netherlands, 1959; pp. 24–96. ISBN 978-1-4832-0088-0.
55. *ISO 8608:1995*; Mechanical Vibration—Road Surface Profiles—Reporting of Measured Data. ISO: Geneva, Switzerland, 1995. Available online: https://www.iso.org/standard/15913.html (accessed on 17 November 2022).
56. Shtessel, Y.; Edwards, C.; Fridman, L.; Levant, A. *Sliding Mode Control and Observation*; Springer: Berlin/Heidelberg, Germany, 2014.
57. Linear Actuator, LA25-42-000A, Technical Documentation. Available online: https://www.sensata.com/sites/default/files/a/sensata-linear-actuator-LA-25-42-drawing.pdf (accessed on 17 November 2022).
58. Linear Encoder with Integrated Converter, LIKA SMK, Technical Documentation. Available online: http://www.lika.pl/pliki_do_pobrania/CAT%20SMK%20E.pdf (accessed on 17 November 2022).
59. Linear Encoder with Sinus/Cosinus Output, LIKA SMS12, Technical Documentation. Available online: http://www.lika.pl/pliki_do_pobrania/CAT%20SMS12%20E.pdf (accessed on 17 November 2022).

60. 9063 CompactRIO Controller, Technical Documentation. Available online: https://www.ni.com/pl-pl/support/model.crio-9063.html (accessed on 17 November 2022).
61. Lee, H.; Utkin, V.I. Chattering Suppression Methods in Sliding Mode Control Systems. *Annu. Rev. Control.* **2007**, *31*, 179–188. [CrossRef]